Scalable Production of Few-Layer Boron Sheets by Liquid-Phase Exfoliation and Their Superior Supercapacitive Performance

Hongling Li,[1,⊥] Lin Jing,[2,⊥] Wenwen Liu,[3] Jinjun Lin,[1] Roland Yingjie Tay,[4] Siu Hon Tsang,[4] and Edwin Hang Tong Teo [1,2,*]

[1]School of Electrical and Electronic Engineering, Nanyang Technological University, 50 Nanyang Avenue, Singapore 639798, Singapore

[2]School of Materials Science and Engineering, Nanyang Technological University, 50 Nanyang Avenue, Singapore 639798, Singapore

[3]Department of Chemical Engineering, Waterloo Institute for Nanotechnology, University of Waterloo, Waterloo, Ontario, Canada N2L 3G1

[4]Temasek Laboratories@NTU, 50 Nanyang Avenue, Singapore 639798, Singapore

*Corresponding Author. *E-mail:* HTTEO@ntu.edu.sg

⊥These two authors contributed equally to this work.

ABSTRACT: Although two-dimensional boron (B) has attracted much attention in electronics and optoelectronics due to its unique physical and chemical properties, in-depth investigations and applications have been limited by the current synthesis techniques. Herein, we demonstrate that high-quality few-layer B sheets can be prepared in large quantities by sonication-assisted liquid-phase exfoliation. By simply varying the exfoliating solvent types and centrifugation speeds, the lateral size and thickness of the exfoliated B sheets can be controllably tuned. Additionally, the exfoliated few-layer B sheets exhibit excellent stability and outstanding dispersion in organic solvents without aggregates for more than 50 days under ambient conditions, owing to the presence of a solvent residue shell on the B sheet surface that provides excellent protection against air oxidation. Moreover, we also demonstrate the use of the exfoliated few-layer B sheets for high-performance supercapacitor electrode materials. This as-prepared device exhibits impressive electrochemical performance with a wide potential window of up to 3.0 V, excellent energy density as high as 46.1 Wh/kg at a power density of 478.5 W/kg and excellent cycling stability with 88.7% retention of the initial specific capacitance after 6000 cycles. This current work not only demonstrates an effective strategy for the synthesis of the few-layer B sheets in a controlled manner but also makes the resulting materials promising for next-generation optoelectronics and energy storage applications.

KEYWORDS: few-layer boron sheet, liquid-phase exfoliation, centrifugation, band gap, supercapacitor, electrode material

Two-dimensional (2D) materials such as graphene,[1,2] transition metal dichalcogenides (TMDs)[3,4] and black phosphorus (BP)[5–11] with exciting optical, phonon and electronic properties that are different from their bulk counterparts, have aroused great interest due to their potential applications in high performance electronic and optoelectronic devices.[3,6,12–14] Among these 2D materials, graphene with high charge carrier mobility has shown great potential for electronics, but the absence of a band gap limits its practical use in many applications.[2,12,15] On the other hand, BP has been most intensively investigated due to its thickness-dependent band gap, high mobility and anisotropic photoelectronic properties, but this material suffers from severe degradation upon air exposure, which restricts its applications in photoelectric and photovoltaic devices.[8,10,16] The recent discovery of atomically thin boron (also called borophene)[17–19] has been shown to be another promising alternative 2D material in many areas of electronics and optoelectronics,[20] due to its fascinating chemical and structural complexity,[21] tunable band gap,[20, 22–24] massless Dirac fermions,[25] high carrier mobility,[26,27] superhardness[24] and superconductivity.[28]

Since 99% pure B was first synthesized in 1909,[29] various low dimensional B allotropes including nanotubes,[30–35] nanocones,[34,36] nanoribbons,[37–40] nanowires,[34,41–43] fullerenes[44] and 2D B sheets[45,46] have been extensively studied. Among them, the 2D B structure is particularly interesting and has recently attracted considerable theoretical attention.[22,46–55] Despite these considerable theoretical achievements, there were only a few experimental studies on 2D B sheets. Recently, Tai *et al*. have successfully synthesized atomically thin 2D B films on copper foils by chemical vapor deposition at low pressures.[17] Xu *et al*. have fabricated 2D B sheets by vapor–solid process *via* thermal decomposition of diborane under a low pressure.[27] Mannix *et al*.[18] and Feng *et al*.[19] have grown 2D borophene and B sheets on silver substrates under ultra-high-vacuum conditions, respectively. However, these methods still encounter various drawbacks such as the need for ultra-high-vacuum/low-pressure

growth, an additional transfer step that inevitably deteriorates the quality of the sheets, limited quantities and insufficient yield, restricting many of their potential applications.[56] Therefore, developing a facile and efficient approach for experimental realization of high-quality few-layer B sheets in large quantities is highly desirable but remains a great challenge. To date, both chemical exfoliation (*e.g.*, lithium intercalation and oxidation)[57] and sonication-assisted liquid-phase exfoliation[5,58–61] have been proven to be effective for the production of large quantities of 2D materials. Compared with chemical exfoliation, sonication-assisted liquid-phase exfoliation without involving intermediate chemical reactions[57,59] is believed to be a more promising option to prepare 2D B sheets, which has not been explored yet.

Herein, we demonstrate a scalable liquid-phase exfoliation technique for the production of high-quality few-layer B sheets with high solubility in dimethylformamide (DMF) and isopropyl alcohol (IPA). By varying the exfoliating solvent types and centrifugation speeds, B sheets with controllable thickness and size can be synthesized. Their morphologies, structures, and chemical compositions were comprehensively characterized by atomic force microscopy (AFM), high-resolution transmission electron microscopy (HRTEM), selected-area electron diffraction (SAED), X-ray diffraction (XRD), X-ray photoelectron spectroscopy (XPS) and electron energy-loss spectroscopy (EELS) analysis. Impressively, the exfoliated B sheets show excellent stability in the exfoliating solvent without aggregates observed even after 50 days of exposure to ambient conditions, which indicates great promise for further processing and applications. As an example, we demonstrated the use of the exfoliated few-layer B sheets for high-performance supercapacitor electrode materials. The as-prepared device can be cycled reversibly in a high potential window of 0–3.0 V and exhibits a maximum specific capacitance of 142.6 F/g with an excellent energy density of 46.1 Wh/kg at a power density of 478.5 W/kg, as well as superior cycling stability (88.7% retention after 6000 cycles). These encouraging results presented here provide the opportunity for the

application of as-prepared few-layer B sheets in design and construction of next-generation high-performance optoelectronics and energy storage devices.

RESULTS AND DISCUSSION

The sonication-assisted liquid-phase exfoliation method was employed to exfoliate few-layer B sheets from bulk B as shown in Figure 1a. DMF, an excellent exfoliating solvent for graphene, boron nitride, and TMDs as well as BP, was chosen as the model solvent to examine its performance for the B exfoliation, while IPA from different chemical family was chosen as a comparison.[58,61–63] Initially, bulk B powder with an average lateral particle size of 2 μm was immersed into DMF/IPA (1 mg mL^{-1}) and was sonicated at 350 W for 4 h. To tailor the concentration and the thickness of the exfoliated B sheets, the sonicated B sheet was then centrifuged at different centrifugation speeds and the corresponding supernatants were carefully collected. Stable, light-brown-colored dispersions in both DMF and IPA solvents can be obtained after centrifugation at 5000 rpm for 30 min. Compared with the bulk B, the DMF-exfoliated B sheets are observed to be almost transparent with dimensions ranging from severeal nanometers to several micrometers (Figure 1b-d), indicating the exfoliation of the bulk B.

In order to determine the dispersed concentration, optical characteristics of the exfoliated B sheet dispersions were investigated by UV-vis spectroscopy (Figure 2). Figure 2a,d show the sonicated B sheet dispersions in DMF (Figure 2a) and IPA (Figure 2d) as well as the corresponding supernatants obtained at different centrifugation speeds of 2000, 5000, and 12000 rpm for 30 min. It is observed that the color of both DMF- and IPA-exfoliated few-layer B sheet dispersions changes from dark brown to light yellow with decreasing the concentration. To calculate the absorption coefficient (α) of the B sheet dispersions, a certain amount of dried B sheet solid was first redispersed in DMF/IPA solution and further diluted a

number of times and the corresponding absorption spectra were recorded (Figure S1a,c; see Materials and Methods for more details). It is worth noting that the absorbance divided by cell length (A/*l*) at wavelength λ = 400 nm for DMF and λ = 504 nm for IPA shows a perfect linear relationship with the concentration (C) (Figure 2b,e), suggesting well-dispersed B sheets in both solutions. These behaviors are well consistent with the Lambert–Beer law, $A/l = \alpha C$, giving an absorption coefficient of α = 704.38 for DMF and α = 977.55 L g^{-1} m^{-1} for IPA. After careful measurements of their absorption spectra, the concentrations of the B sheet dispersions prepared at different centrifugation speeds of 2000, 5000, and 12000 rpm for 30 min were calculated to be 1.16, 0.05, and 0.01 mg/mL in DMF and 0.46, 0.09, and 0.004 mg/mL in IPA, respectively. The Tyndall effect was observed for both the DMF- and IPA-exfoliated B sheet dispersions after centrifugation at 5000 rpm for 30 min (insets of Figure 2b,e), indicating the colloidal nature of the as-prepared dispersion. The optical band gap (E_g) of the exfoliated B sheets was calculated according to $\alpha = C\,(E - E_g)^{1/2}/E$, where α is the absorption coefficient, C is a constant, and E is the photon energy. As shown in Figure 2c,f, the corresponding approximate E_g for DMF-exfoliated B sheet dispersions after centrifugation at 5000 and 12000 rpm for 30 min were 3.6 and 3.8 eV, respectively, while for IPA-exfoliated B sheet dispersions at the same conditions they were estimated to be 2.6 and 3.8 eV. All four values are much higher than that of the bulk B (~1.5 eV).[22] It is worth noting that the B sheet dispersions in DMF and IPA exhibit the same E_g value (3.8 eV) after centrifugation at a higher speed of 12000 rpm, while the former shows a much higher E_g value than the latter when a relatively lower centrifugation speed of 5000 rpm was used. The corresponding E_g for redispered B sheets in DMF and IPA with different concentrations have also been calculated (Figure S1b,d). It is observed that the redispersed B sheet dispersions in DMF mainly show E_g ranging from 3.6 to 4.0 eV, which is similar to those of the centrifuged samples at 5000 and 12000 rpm. However, the redispersed B sheet dispersions in IPA exhibit

nonregular optical properties and the E_g varies with the increase of the concentration, which are signs of reaggregation of B sheets. These results indicate that the DMF-exfoliated B sheets show better stability and redispersion properties than those of the IPA-exfoliated B sheets.

AFM was employed to further explore the thickness and area distributions of the DMF- and IPA-exfoliated B sheets as shown in Figure 3. The existence of few-layer curved and flat B sheets prepared in DMF and IPA can be clearly seen in the representative AFM topographic images (Figure 3a,d). Statistical AFM shows that the average thickness and area of the DMF-exfoliated B sheets are 1.8 nm (corresponding to *ca*. 4 B layers, Figure 3b) and 19827 nm^2 (Figure 3c), respectively, while the IPA-exfoliated B sheets possess a larger mean thickness of 4.7 nm (corresponding to *ca.* 11 B layers, Figure 3e) and smaller mean area of 1791 nm^2 (Figure 3f). It is noted that DMF-exfoliated B sheets show larger lateral size (~11 times larger) and thinner layers (~ 82% of the observed sheets have less than 6 layers) compared with IPA-exfoliated B sheets at the same conditions. These results suggest that the thickness and area distributions of the exfoliated B sheets can be well controlled by varying the exfoliating solvents used.

Next, TEM, SAED, EELS, and XRD were performed to examine the morphology and crystallinity of the exfoliated B sheets. As shown in Figure 4a, large quantities of randomly oriented few-layer thin B sheets and a small number of atomically thin B sheets with lateral size of 100-200 nm were found for DMF-exfoliated B sheet sample, which is consistent with the above-mentioned AFM results. The SAED pattern (Figure S2), the corresponding fast Fourier transform (FFT) diffraction pattern of the representative individual B sheet (inset of Figure 4b), and the HRTEM observation (Figure 4c) further demonstrate the crystalline nature of the few-layer B sheets, showing a clear interference fringe with a d-spacing of 0.504 nm, corresponding to the (104) plane of a β-rhombohedral B structure.[64] The uniform

lattice fringes shown in Figure 4b,c suggest that the crystalline state of the few-layer B sheets after liquid-phase exfoliation process is pristine. Figure 4d-f show the TEM and HRTEM images of the IPA-exfoliated B sheets. The B sheets exfoliated by IPA were observed with relatively thicker layers compared with the DMF-exfoliated B sheets. Two individual IPA-exfoliated B sheets exhibit lattice spacings of 0.427 and 0.435 nm, corresponding to the (015) and (202) planes of the B crystal, respectively, which is different from those of DMF-exfoliated B sheets (Figure 4e,f).[64] Figure 4g,l show a high angle annular dark field (HAADF) scanning TEM (STEM) image of an individual DMF-exfoliated and IPA-exfoliated B sheet. Their corresponding EELS elemental mapping images (Figure 4h-k and m-p) show the uniform distribution of B element throughout the whole sheet with an observable shell consisting of C, N and O elements. This can be further verified by the corresponding EELS spectra (Figure 4q), which exhibit a characteristic boron K-shell ionization edge at ~188 eV.[27,37] The amounts of the B, C, N and O extracted from the EELS spectra were 97.39 at.%, 0.78 at.%, 1.17 at.% and 0.66 at.% for the DMF-exfoliated B sheet and 96.72 at.%, 0.65 at.%, 0.85 at.% and 1.78 at.% for the IPA-exfoliated B sheet, respectively. The existence of small amounts of C, N, and O is likely due to the surface contamination occurring during exposure to air atmosphere and the exfoliating solvent. The crystalline structure and phase purity of the bulk B before and after liquid-phase exfoliation were further verified by XRD (Figure 4r). All four samples display similar XRD patterns, and most of their major peaks can be indexed to the β-rhombohedral B (JCPDF 00-031-0207),[64] indicating both the DMF- and IPA-exfoliated few-layer B sheets retain the crystallinity of the original bulk B. These results are in good agreement with the structural parameters obtained by HRTEM.

XPS was utilized to further investigate the surface composition and chemical state of the B before and after sonication-assisted liquid-phase exfoliation. Figure 5a shows the XPS survey scan spectra for binding energies ranging from 0 to 600 eV. In addition to the B peaks, peaks

corresponding to C, O, and N were also detected for all four samples. The C, O, and a small amount of N species mainly arise from the surface contamination when exposed to air atmosphere as mentioned earlier. It is noted that there is no obvious change in the B content for all four B samples, indicating the surface composition can be well retained after the sonication-assisted liquid-phase exfoliation process. Since XPS is a surface analysis tool, it is not surprising that higher apparent O and C concentrations are found as compared to scanning electron microscopy (SEM)-energy dispersive X-ray (EDX) for bulk B (see Figure S3 for more details) and EELS for the exfoliated B sheets, respectively.[37] Figure 5b shows the high-resolution B 1s spectra of the four different B samples. Three peaks centered at 192.1, 189.1, and 187.7 eV, respectively, can be resolved in the B 1s spectrum of bulk B, indicating that there are three types of bonding structures of B. The main component at 187.7 eV corresponded to a B-B bond, which is consistent with the reported value obtained from bulk B (187.3-187.9 eV).[37] The higher binding energy components at 189.1 and 192.1 eV are mainly due to the oxidation of B. The peak centered at 189.1 can be assigned to the B-O bond in a boron-rich oxide, while the small peak located at 192.1 eV can be an indication of the formation of B_2O_3. It should be mentioned that the component at 189.1 eV may also arise from the formation of a B-C bond due to exposure to air or solvent. Notably, the extracted ratio of the B-B peak in the above-mentioned bonding structures of B is ~72.4%, indicating the existence of a small amount of O-containing and/or C-containing defects in the bulk B. These defects are expected to be more active and thus more easily attached by the exfoliating reagent molecules, thereby allowing more effective exfoliation and fragmentation of bulk B during the sonication-assisted liquid-phase exfoliation process. It is noted that the main binding energy peaks for the B component are slightly shifted (187.4 eV) compared with the bulk value, which is similar to the previously reported phenomenon for 2D B sheets.[17,19] In addition, the small peak corresponding to B_2O_3 disappeared for all the samples after the

exfoliation process due to their interactions with the exfoliating solvent, while another component centered at 190.4 eV was found, possibly attributive to the formation of B-N bonds due to the air contamination. Figure 5c shows the high-resolution C 1s spectra of the four different B samples. All the C 1s spectra can be fitted to four components at around 282.8, 284.8, 286.3, and 288.8 eV, which can be assigned to the C-B, C-C, C-N/C-O, and C=O bonds, respectively. Importantly, the measured ratios of the C-B peak for exfoliated few-layer B sheets in DMF and IPA are only ~0.033 and ~0.058, respectively, indicating that most B atoms remain intact after the sonication-assisted liquid-phase exfoliation process. This is also very consistent with the EELS mapping spectra, where a shell mainly consisting of C and O elements is observed on the edges of the B sheets.

In addition to the excellent optical properties, the stability of an exfoliated 2D material is also closely related to its practical electronic and optoelectronic applications.[5,10] Therefore, the stability of the DMF-exfoliated few-layer B sheet dispersions was examined by monitoring their optical absorption property changes before and after 50 days of exposure to ambient conditions (Figure 6). Figure 6a,b show the optical absorption spectra of fresh exfoliated B sheet dispersions in DMF after centrifugation at 5000 and 12000 rpm for 30 min and the corresponding dispersions after 50 days of exposure to ambient conditions, respectively. As expected, there is almost no change in the spectra of the DMF-exfoliated B sheet dispersions, indicating excellent stability of the as-prepared colloid. This can be attributed to the presence of a solvent residue shell on the B sheet surface that provides excellent protection against air oxidation. This is also supported by an obvious Tyndall effect of the B sheet dispersion without noticeable aggregates after 50 days of exposure to ambient conditions (inset of Figure 6a) and the lack of obvious changes in the approximate optical band gap (inset of Figure 6b).

Very recently, a few theoretical studies have shown that the 2D B sheet as a member of the 2D materials is a highly promising electrode material for supercapacitors and batteries due to its unique properties such as excellent electronic conductivity, high specific surface area, low mass density, and strong mechanical property.[20,65] As an example, a symmetric two-electrode cell assembled in a glovebox with DMF-exfoliated few-layer B sheets as the active material is employed to evaluate its electrochemical performance. Figure 7a shows cyclic voltammetry (CV) curves of the as-prepared coin cell under various voltage windows in an ionic liquid, 1-butyl-3-methylimidazolium hexafluorophosphate, at a scan rate of 10 mV/s. It can be observed that the CV curve still retains a rectangular-like shape even at a voltage window of up to 3 V, indicating a good capacitive behavior of the as-prepared supercapacitor with a stable and large voltage window in ionic liquid electrolyte.[66,67] In addition, the specific capacitance greatly increases from 91.6 F/g to 142.6 F/g with an increase of potential window from 1.0 to 3.0 V. Given the idea that the energy density of an electrochemical capacitor is directly proportional to the square of its cell voltage and the specific power density is proportional to its cell voltage, the stable and large potential window will not only enhance the energy density of the cell but also reduce the number of cells in series to meet the desired output voltage. Therefore, the potential window of 3.0 V is used in subsequent experiments to evaluate the overall electrochemical performance of the cell. As shown in Figure 7b, all the CV curves of the DMF-exfoliated few-layer B sheets exhibit a nearly rectangle-like shape even at a scan rate as high as 100 mV/s, indicating a pretty good capacitive behavior and a fast charge/discharge property of the as-prepared B sheets in ionic liquid electrolyte.[68]

The electrochemical performance of the as-prepared supercapacitor is further examined by galvanostatic charge/discharge measurements at various current densities (Figure 7c). All the charge/discharge curves show high symmetry and nearly linear slopes without observable voltage (IR) drop, revealing relatively small equivalent series resistance of the cell.[67,68] The

specific capacitances and corresponding cell capacitances of the as-prepared supercapacitor at different current densities are presented in Figure 7d. The maximum specific capacitance of 147.6 F/g is achieved at a current density of 0.3 A/g, which is higher than the supercapacitor based on bulk B (specific capacitance of 41.7 F/g, Figure S4) and those of reported carbon-based materials in ionic liquid electrolyte including reduced graphene nanosheets (RGO),[69,70] RGO-CMK-5 composite and porous carbon.[71,72] More importantly, the specific capacitance of the as-assembled supercapacitor still maintains 98.3 F/g with a capacitance retention of 66.6% when the current density is increased 20-fold from 0.3 to 6.0 A/g, demonstrating its good rate capability. The high specific capacitance and good rate capability of the as-prepared supercapacitor are mainly attributed to the excellent electronic conductivity of the exfoliated B sheets, which can provide an effective charge transport pathway during the charge/discharge process.[73,74] Meanwhile, the puckered morphology and layer structure of the B sheets offer abundant active sites with the full surface exposed and enable fast access of electrolyte ions.[75] Additionally, it is worth noting that the specific capacitances gradually decrease with the increase of current densities, which is due to the low utilization efficiency of active materials, resulting from slower ion diffusion of ionic liquid at higher current density.[66,69]

Good cycling stability is another important characteristic for the practical application of supercapacitors. Figure 7e shows the capacitance retention ratio of the as-assembled supercapacitor measured at a scan rate of 50 mV/s for 6000 cycles. It is noted that the specific capacitance of the as-prepared supercapacitor slightly increases in the first 200 cycles and still remains 88.7% even after 6000 cycles, indicating excellent cycling stability. Encouragingly, this retention ratio is comparable to or better than those of reported carbon-based supercapacitors in ionic liquid such as RGO||RGO (93% after 1500 cycles),[76] RGO-CMK-5 composite||RGO-CMK-5 composite (90% after 2000 cycles),[71] and RGO-

RuO_2||RGO-RuO_2 (70% after 2000 cycles).[77] It should be mentioned that a slight decrease of capacitance observed during the cycling process is probably attributed to pulverization and loss of electrical contact between B sheets and current collector.[78] This can be well supported by an electrochemical impedance spectroscopy (EIS) tests of the as-prepared device before and after 6000 cycles (Figure 7f). Noticeably, the EIS spectra are similar in terms of the curve shape with a semicircle at high frequency and a linear line at low frequency. However, the equivalent series resistance (the value of the first intercept point of the Nyquist plot with a real axis) increases from 19.8 ohm to 22.4 ohm after 6000 cycles, demonstrating a slight increase of the internal resistance of the device. Moreover, it is also observed that the charge transfer resistance (the value of the diameter of the semicircle) becomes larger after cycling test, indicating a relatively slow ion transport within the supercapacitor, which are probably related to the reduced contact area at the electrode/electrolyte interface.

To further demonstrate the performance of the as-obtained supercapacitor based on B nanosheets, a Ragone plot, showing the relationship of energy density and power density, is plotted in Figure 7g. The energy density can reach 46.1 Wh/kg at a power density of 478.5 W/kg and still maintains 29.1 Wh/kg at a power density of 22616.2 W/kg, which is higher than the required power target of the partnership for a next-generation vehicle (15.0 kW/kg),[67] indicating its potential application as power supply for hybrid vehicles. Furthermore, the maximum energy density of 46.1 Wh/kg achieved is comparable to or higher than those of carbon-based supercapacitors in ionic liquid electrolyte, including active carbon//active carbon, [79] cellulose derived carbon nanofiber-activated carbon (NCAC) composite||NCAC composite,[79] RGO||RGO,[76] RGO-CMK-5 composite||RGO-CMK-5 composite,[71] graphitic biomass carbon||graphitic biomass carbon,[80] and porous carbon||porous carbon.[81] Such an excellent capacitive performance is ascribed to the high specific capacitance of B sheets and the use of an ionic liquid electrolyte with a large potential

window. To evaluate the practical applications, the as-prepared supercapacitor is used to drive some small electronic devices. Excitingly, one obtained coin cell can efficiently power one red LED light (Figure 7h) and drive one mini-fan (Figure 7i) after charging few seconds, respectively. These encouraging results presented here provide the opportunity for the application of B sheets in the design and construction of high-performance supercapacitors and other energy storage devices.

CONCLUSIONS

In summary, we have demonstrated an effective approach to produce few-layer B sheets in large quantities by liquid-phase exfoliation of bulk B. By choosing DMF and IPA as the exfoliating solvents, few-layer B sheets with controllable size (average area in DMF and IPA is 19827 and 1791 nm^2, respectively) and thickness (average thickness in DMF and IPA is 1.8 and 4.7 nm, respectively) can be prepared. The as-prepared few-layer B sheet dispersion with high solubility in DMF (up to 1.16 mg/mL) was stable for at least 50 days after exposure to ambient conditions. In addition, the approximate optical band gaps for DMF- and IPA-exfoliated B sheet dispersions after centrifugation at 5000 rpm for 30 min were calculated to be 3.6 and 2.6 eV, respectively. More significantly, the DMF-exfoliated few-layer B sheets have been applied as supercapacitor electrode materials and the as-prepared device possesses a potential window as high as 3.0 V and exhibits a maximum specific capacitance of 142.6 F/g at a current density of 0.3 A/g. Furthermore, such a device also shows an impressive energy density of 46.1 Wh/kg at a power density of 478.5 W/kg and an excellent cycling stability, *i.e.*, 88.7% retention of the initial specific capacitance even after 6000 cycles. This work provides the possibility for the few-layer B sheets to be formed into thin films and composites in a large-scale with a broad range of potential applications such as flexible electronics, optoelectronics, and energy storage devices.

MATERIALS AND METHODS

Materials. Boron powder (95%) with an average particle size of 2 μm was purchased from Merck. N,N-Dimethylformamide (ACS, 99.8+%) was purchased from Alfa Aesar. Isopropyl alcohol was purchased from Best Chemical Co (S) Pte Ltd. All chemicals were used as received without further purification.

Preparation of Few-Layer B Sheet Dispersion. Typically, 100 mg of B powder was added into 100 mL of DMF or IPA solution. The mixture was then sonicated at 350 W for 4 h, with 1 s ultrasonication and 2 s pause using a probe-type sonicator (JY92-IIN, Scientiz, China). The container was sealed with Teflon tape to suppress additional air contamination during the ultrasonic process. Afterward, the supernatant was decanted and centrifuged at 2000-5000 rpm for 30 min (Kubota 3740 centrifuge, Kubota, Japan) to remove unexfoliated B particles. Finally, the resulting B sheet dispersion (supernatant) was either carefully collected for further morphological and structural characterization or subjected to further centrifugation at a higher speed of 12000 rpm for 30 min for sediment collection.

Characterization. Morphology and nanostructure of bulk B powder and the as-prepared few-layer B sheets were characterized by SEM (LEO 1550), TEM (Tecnai G2 F20 X-Twin), and SAED. X-ray diffraction (Shimadzu XRD-6000) was used to study their crystallinity. Their composition and chemical state were determined by X-ray photoelectron spectroscopy (XPS, PHI Quantera II) and electron energy-loss spectroscopy (EELS). XPS was performed using monochromated Al Kα X-rays (1486.6 eV), and the binding energy calibration was referenced to C 1s at 284.8 eV. The absorption spectra of the DMF- and IPA-exfoliated B sheet dispersions were measured using a UV-vis spectrophotometer (Shimadzu 2450) at room temperature. The thickness and area of individual B sheets were measured with AFM (Asylum Research, MFP-3D). AFM samples were prepared by dropping the B sheet dispersions onto SiO_2/Si substrates followed by drying under vacuum at 50 ºC for 8 h. TEM

samples were prepared by directly dropping the B sheet dispersions onto holey carbon TEM grids (Cu, 400 mesh) followed by drying under vacuum at 50 ºC for 8 h.

Determination of the Absorption Coefficient of B Sheet Dispersions. Typically, 50 mL of B sheet dispersion was further centrifuged at 12000 rpm for 30-60 min and the resulting solid was collected, followed by drying under vacuum at 50 ºC for 8 h. A certain amount of dried B product (2.5 mg for DMF and 2 mg for IPA) was redispersed in 5 mL of DMF/IPA solution with mild bath sonication for 5 min, and then a colloid solution was obtained. Each of these dispersions was diluted a number of times, and the corresponding absorption spectra were recorded. The optical absorbance per cell length (A/*l*) was determined from optical absorbance spectra at 400 nm for DMF solution and 503 nm for IPA solution, respectively. Using Lambert–Beer's law ($A/l = \alpha C$, where α is the extinction coefficient), the B extinction coefficient was extracted from the slope of a plot of A/*l* versus concentration.

Electrode Preparation and Electrochemical Characterization. The preparation process of electrode is briefly described as follows. First, boron nanosheets, active carbon, and 1 wt % poly(tetrafluoroethylene) with a mass ratio of 85:5:10 were mixed uniformly by adding some drops of ethanol in a mortar. Then, the obtained slurry was coated onto nickel foam and dried at 50 ºC in a vacuum oven for 10 h. Next, the electrode was pressed at 10 MP to make a good electric connection. After that, a coin cell (CR 2032) was assembled in a glovebox using the as-prepared electrode as working electrode and 1-butyl-3-methylimidazolium hexafluorophosphate as the electrolyte. The electrochemical performances were characterized by a VMP3 potentiostat/galvanostat (Bio-Logic LLC, Knoxville, TN, USA) at room temperature. The CV measurement was performed with various potential windows from 0.0 to 3.0 V at different scan rates varying from 10 to 100 mV/s. Galvanostatic charge/discharge tests were collected at different current densities ranging from 0.3 to 6 A/g. The EIS was carried out in the frequency ranging from 100 kHz to 0.05 Hz at open circuit potential with an

ac perturbation of 5 mV. The specific capacitance of the cell (C_{cell}) was calculated from the discharge curve by the formula

$$C_{cell} = \frac{I \cdot \Delta t}{m \cdot \Delta V} \quad (1)$$

The specific capacitance of the electrode (C_{sp}) was calculated from the discharge curve by the formula

$$C_{sp} = 4C_{cell} = \frac{4 \cdot I \cdot \Delta t}{m \cdot \Delta V} \quad (2)$$

The specific energy density and power density were defined respectively by

$$E = \frac{C_{cell} \cdot \Delta V}{7.2} \quad (3)$$

And

$$P = \frac{E \times 3600}{\Delta t} \quad (4)$$

where, I is the charge/discharge current (A/g), Δt is the discharge time (s), ΔV is the potential window during the discharge process after internal resistance drop (V), m is the mass of two electrode materials (g), C_{cell} is the specific capacitance of the device (F/g), C_{sp} is the specific capacitance of the electrode (F/g), E is the energy density (Wh/kg) and P is the power density (W/kg).

CONFLICT OF INTEREST

The authors declare no competing financial interest.

ACKNOWLEDGEMENTS

The authors gratefully acknowledge the funding support from Singapore Ministry of Education Academic Research Fund Tier 2 No. MOE2013-T2-2-050.

SUPPORTING INFORMATION

Optical absorption spectra and the corresponding optical band gap of redispersed B sheet dispersions in DMF and IPA with different concentrations; Typical TEM image of the few-layer B sheets exfoliated in DMF at lower magnification and the corresponding SAED pattern; Typical SEM, corresponding elemental mapping images of B, C, O, and EDX spectrum of the bulk B; Comparison of electrochemical performance of bulk B and DMF-exfoliated few-layer B sheets based supercapacitor in ionic liquid electrolyte.

REFERENCES

(1) Nair, R. R.; Blake, P.; Grigorenko, A. N.; Novoselov, K. S.; Booth, T. J.; Stauber, T.; Peres, N. M.; Geim, A. K. Fine Structure Constant Defines Visual Transparency of Graphene. *Science* **2008**, *320*, 1308.

(2) Orlita, M.; Faugeras, C.; Plochocka, P.; Neugebauer, P.; Martinez, G.; Maude, D. K.; Barra, A. L.; Sprinkle, M.; Berger, C.; de Heer, W. A.; Potemski, M. Approaching the Dirac Point in High-Mobility Multilayer Epitaxial Graphene. *Phys. Rev. Lett.* **2008**, *101*, 267601.

(3) Wang, Q. H.; Kalantar-Zadeh, K.; Kis, A.; Coleman, J. N.; Strano, M. S. Electronics and Optoelectronics of Two-Dimensional Transition Metal Dichalcogenides. *Nat. Nanotechnol.* **2012**, *7*, 699–712.

(4) Chhowalla, M.; Shin, H. S.; Eda, G.; Li, L. J.; Loh, K. P.; Zhang, H. The Chemistry of Two-Dimensional Layered Transition Metal Dichalcogenide Nanosheets. *Nat. Chem.* **2013**, *5*, 263–275.

(5) Hanlon, D.; Backes, C.; Doherty, E.; Cucinotta, C. S.; Berner, N. C.; Boland, C.; Lee, K.; Harvey, A.; Lynch, P.; Gholamvand, Z.; Zhang, S.; Wang, K.; Moynihan, G.; Pokle, A.; Ramasse, Q. M.; McEvoy, N.; Blau, W. J.; Wang, J.; Abellan, G.; Hauke, F.; *et al*. Liquid Exfoliation of Solvent-Stabilized Few-Layer Black Phosphorus for Applications Beyond Electronics. *Nat. Commun.* **2015**, *6*, 8563.

(6) Li, L.; Yu, Y.; Ye, G. J.; Ge, Q.; Ou, X.; Wu, H.; Feng, D.; Chen, X. H.; Zhang, Y. Black Phosphorus Field-Effect Transistors. *Nat. Nanotechnol.* **2014**, *9*, 372–377.

(7) Illarionov, Y. Y.; Waltl, M.; Rzepa, G.; Kim, J. S.; Kim, S.; Dodabalapur, A.; Akinwande, D.; Grasser, T. Long-Term Stability and Reliability of Black Phosphorus Field-Effect Transistors. *ACS Nano* **2016**, *10*, 9543–9549.

(8) Wood, J. D.; Wells, S. A.; Jariwala, D.; Chen, K. S.; Cho, E.; Sangwan, V. K.; Liu, X.; Lauhon, L. J.; Marks, T. J.; Hersam, M. C. Effective Passivation of Exfoliated Black Phosphorus Transistors Against Ambient Degradation. *Nano Lett.* **2014**, *14*, 6964–6970.

(9) Chen, L.; Zhou, G.; Liu, Z.; Ma, X.; Chen, J.; Zhang, Z.; Ma, X.; Li, F.; Cheng, H. M.; Ren, W. Scalable Clean Exfoliation of High-Quality Few-Layer Black Phosphorus for a Flexible Lithium Ion Battery. *Adv. Mater.* **2016**, *28*, 510–517.

(10) Kang, J.; Wood, J. D.; Wells, S. A.; Lee, J. H.; Liu, X.; Chen, K. S.; Hersam, M. C. Solvent Exfoliation of Electronic-Grade, Two-Dimensional Black Phosphorus. *ACS Nano* **2015**, *9*, 3596–3604.

(11) Buscema, M.; Groenendijk, D. J.; Blanter, S. I.; Steele, G. A.; van der Zant, H. S.; Castellanos–Gomez, A. Fast and Broadband Photoresponse of Few-Layer Black Phosphorus Field-Effect Transistors. *Nano Lett.* **2014**, *14*, 3347–3352.

(12) Fiori, G.; Bonaccorso, F.; Iannaccone, G.; Palacios, T.; Neumaier, D.; Seabaugh, A.; Banerjee, S. K.; Colombo, L. Electronics Based on Two-Dimensional Materials. *Nat. Nanotechnol.* **2014**, *9*, 768–779.

(13) Fu, Q.; Bao, X. Surface Chemistry and Catalysis Confined under Two-Dimensional Materials. *Chem. Soc. Rev.* **2017**, *46*, 1842–1874.

(14) Mannix, A. J.; Kiraly, B.; Hersam, M. C.; Guisinger, N. P. Synthesis and Chemistry of Elemental 2D Materials. *Nat. Rev. Chem.* **2017**, *1*, 0014.

(15) Chen, J. H.; Jang, C.; Xiao, S.; Ishigami, M.; Fuhrer, M. S. Intrinsic and Extrinsic Performance Limits of Graphene Devices on SiO_2. *Nat. Nanotechnol.* **2008**, *3*, 206–209.

(16) Li, L.; Kim, J.; Jin, C.; Ye, G. J.; Qiu, D. Y.; da Jornada, F. H.; Shi, Z.; Chen, L.; Zhang, Z.; Yang, F.; Watanabe, K.; Taniguchi, T.; Ren, W.; Louie, S. G.; Chen, X. H.; Zhang, Y.; Wang, F. Direct Observation of The Layer-Dependent Electronic Structure in Phosphorene. *Nat. Nanotechnol.* **2016**, *12*, 21–25.

(17) Tai, G. A.; Hu, T. S.; Zhou, Y. G.; Wang, X. F.; Kong, J. Z.; Zeng, T.; You, Y. C.; Wang, Q. Synthesis of Atomically Thin Boron Films on Copper Foils. *Angew. Chem. Int. Ed.* **2015**, *54*, 15473–15477.

(18) Mannix, A. J.; Zhou, X. F.; Kiraly, B.; Wood, J. D.; Alducin, D.; Myers, B. D.; Liu, X. L.; Fisher, B. L.; Santiago, U.; Guest, J. R.; Yacaman, M. J.; Ponce, A.; Oganov, A. R.; Hersam, M. C.; Guisinger, N. P. Synthesis of Borophenes: Anisotropic, Two-Dimensional Boron Polymorphs. *Science* **2015**, *350*, 1513–1516.

(19) Feng, B. J.; Zhang, J.; Zhong, Q.; Li, W. B.; Li, S.; Li, H.; Cheng, P.; Meng, S.; Chen, L.; Wu, K. H. Experimental Realization of Two-Dimensional Boron Sheets. *Nat. Chem.* **2016**, *8*, 563–568.

(20) Zhang, X.; Hu, J.; Cheng, Y.; Yang, H. Y.; Yao, Y.; Yang, S. A. Borophene as an Extremely High Capacity Electrode Material for Li-Ion and Na-Ion Batteries. *Nanoscale* **2016**, *8*, 15340–15347.

(21) Oganov, A. R.; Chen, J.; Gatti, C.; Ma, Y.; Ma, Y.; Glass, C. W.; Liu, Z.; Yu, T.; Kurakevych, O. O.; Solozhenko, V. L. Ionic High-Pressure Form of Elemental Boron. *Nature* **2009**, *460*, 292.

(22) Wu, X.; Dai, J.; Zhao, Y.; Zhuo, Z.; Yang, J.; Zeng, X. C. Two-Dimensional Boron Monolayer Sheets. *ACS Nano* **2012**, *6*, 7443–7453.

(23) Ogitsu, T.; Schwegler, E.; Galli, G. β-Rhombohedral Boron: at The Crossroads of The Chemistry of Boron and The Physics of Frustration. *Chem. Rev.* **2013**, *113*, 3425–3449.

(24) Zarechnaya, E. Y.; Dubrovinsky, L.; Dubrovinskaia, N.; Filinchuk, Y.; Chernyshov, D.; Dmitriev, V.; Miyajima, N.; El Goresy, A.; Braun, H. F.; Van Smaalen, S.; Kantor, I.; Kantor, A.; Prakapenka, V.; Hanfland, M.; Mikhaylushkin, A. S.; Abrikosov, I. A.; Simak, S. I. Superhard Semiconducting Optically Transparent High Pressure Phase of Boron. *Phys. Rev. Lett.* **2009**, *102*, 185501.

(25) Zhou, X.-F.; Dong, X.; Oganov, A. R.; Zhu, Q.; Tian, Y. J; Wang, H.-T. Semimetallic Two-Dimensional Boron Allotrope with Massless Dirac Fermions. *Phys. Rev. Lett.* **2014**, *112*, 085502.

(26) Boustani, I. New Boron Based Nanostructured Materials. *J. Phys. Chem. C* **1999**, *110*, 3176–3185.

(27) Xu, J. Q.; Chang, Y. Y.; Gan, L.; Ma, Y.; Zhai, T. Y. Ultrathin Single-Crystalline Boron Nanosheets for Enhanced Electro-Optical Performances. *Adv. Sci.* **2015**, 2, 1500023.

(28) Penev, E. S.; Kutana, A.; Yakobson, B. I. Can Two-Dimensional Boron Superconduct? *Nano Lett.* **2016**, *16*, 2522–2526.

(29) Weintraub, E. Preparation and Properties of Pure Boron. *Trans. Am. Electrochem. Soc.* **1909**, *16*, 165–184.

(30) Ciuparu, D.; Klie, R. F.; Zhu, Y. M.; Pfefferle, L. Synthesis of Pure Boron Single-Wall Nanotubes. *J. Phys. Chem. B* **2004**, *108*, 3967–3969.

(31) Patel, R. B.; Chou, T.; Iqbal, Z. Synthesis of Boron Nanowires, Nanotubes, and Nanosheets. *J. Nanomater.* **2015**, *2015*, 243925.

(32) Liu, F.; Shen, C.; Su, Z.; Ding, X.; Deng, S.; Chen, J.; Xu, N.; Gao, H. Metal-Like Single Crystalline Boron Nanotubes: Synthesis and *in Situ* Study on Electric Transport and Field Emission Properties. *J. Mater. Chem.* **2010**, *20*, 2197–2205.

(33) Tang, H.; Ismail-Beigi, S. Novel Precursors for Boron Nanotubes: The Competition of Two-Center and Three-Center Bonding in Boron Sheets. *Phys. Rev. Lett.* **2007**, *99*, 115501.

(34) Tian, J.; Xu, Z.; Shen, C.; Liu, F.; Xu, N.; Gao, H. J. One-Dimensional Boron Nanostructures: Prediction, Synthesis, Characterizations, and Applications. *Nanoscale* **2010**, *2*, 1375–1389.

(35) Bezugly, V.; Kunstmann, J.; Grundkotter-Stock, B.; Frauenheim, T.; Niehaus, T.; Cuniberti, G. Highly Conductive Boron Nanotubes: Transport Properties, Work Functions, and Structural Stabilities. *ACS Nano* **2011**, *5*, 4997–5005.

(36) Wang, X. J.; Tian, J. F.; Yang, T. Z.; Bao, L. H.; Hui, C.; Liu, F.; Shen, C. M.; Gu, C. Z.; Xu, N. S.; Gao, H. J. Single Crystalline Boron Nanocones: Electric Transport and Field Emission Properties. *Adv. Mater.* **2007**, *19*, 4480–4485.

(37) Xu, T. T.; Zheng, J. G.; Wu, N. Q.; Nicholls, A. W.; Roth, J. R.; Dikin, D. A.; Ruoff, R. S. Crystalline Boron Nanoribbons: Synthesis and Characterization. *Nano Lett.* **2004**, *4*, 963–968.

(38) Liu, Y. X.; Dong, Y. J.; Tang, Z. Y.; Wang, X. F.; Wang, L.; Hou, T. J.; Lin, H. P.; Li, Y. Y. Stable and Metallic Borophene Nanoribbons from First-Principles Calculations. *J. Mater. Chem. C* **2016**, *4*, 6380–6385.

(39) Liu, M.; Artyukhov, V. I.; Yakobson, B. I. Mechanochemistry of One-Dimensional Boron: Structural and Electronic Transitions. *J. Am. Chem. Soc.* **2017**, *139*, 2111–2117.

(40) Garcia-Fuente, A.; Carrete, J.; Vega, A.; Gallego, L. J. What will Freestanding Borophene Nanoribbons Look Like? An Analysis of Their Possible Structures, Magnetism and Transport Properties. *Phys. Chem. Chem. Phys.* **2017**, *19*, 1054–1061.

(41) Otten, C. J.; Lourie, O. R.; Yu, M. F.; Cowley, J. M.; Dyer, M. J.; Ruoff, R. S.; Buhro, W. E. Crystalline Boron Nanowires. *J. Am. Chem. Soc.* **2002**, *124*, 4564–4565.

(42) Zhang, Y. J.; Ago, H.; Yumura, M.; Ohshima, S.; Uchida, K.; Komatsu, T.; Iijima, S. Study of The Growth of Boron Nanowires Synthesized by Laser Ablation. *Chem. Phys. Lett.* **2004**, *385*, 177–183.

(43) Liu, F.; Gan, H.; Tang, D. M.; Cao, Y.; Mo, X.; Chen, J.; Deng, S.; Xu, N.; Golberg, D.; Bando, Y. Growth of Large-Scale Boron Nanowire Patterns with Identical Base-Up Mode and *in Situ* Field Emission Studies of Individual Boron Nanowire. *Small* **2014**, *10*, 685–693.

(44) Zhai, H. J.; Zhao, Y. F.; Li, W. L.; Chen, Q.; Bai, H.; Hu, H. S.; Piazza, Z. A.; Tian, W. J.; Lu, H. G.; Wu, Y. B.; Mu, Y. W.; Wei, G. F.; Liu, Z. P.; Li, J.; Li, S. D.; Wang, L. S. Observation of an All-Boron Fullerene. *Nat. Chem.* **2014**, *6*, 727–731.

(45) Tsai, H. S.; Hsiao, C. H.; Lin, Y. P.; Chen, C. W.; Ouyang, H.; Liang, J. H. Fabrication of Multilayer Borophene on Insulator Structure. *Small* **2016**, *12*, 5251–5255.

(46) Sun, X.; Liu, X.; Yin, J.; Yu, J.; Li, Y.; Hang, Y.; Zhou, X.; Yu, M.; Li, J.; Tai, G.; Guo, W. Two-Dimensional Boron Crystals: Structural Stability, Tunable Properties, Fabrications and Applications. *Adv. Funct. Mater.* **2017**, *27*, 1603300.

(47) Piazza, Z. A.; Hu, H. S.; Li, W. L.; Zhao, Y. F.; Li, J.; Wang, L. S. Planar Hexagonal B(36) as a Potential Basis for Extended Single-Atom Layer Boron Sheets. *Nat. Commun.* **2014**, *5*, 3113.

(48) Albert, B.; Hillebrecht, H. Boron: Elementary Challenge for Experimenters and Theoreticians. *Angew. Chem. Int. Ed.* **2009**, *48*, 8640–8668.

(49) Penev, E. S.; Bhowmick, S.; Sadrzadeh, A.; Yakobson, B. I. Polymorphism of Two-Dimensional Boron. *Nano Lett.* **2012**, *12*, 2441–2445.

(50) Liu, H.; Gao, J.; Zhao, J. From Boron Cluster to Two-Dimensional Boron Sheet on Cu(111) Surface: Growth Mechanism and Hole Formation. *Sci. Rep.* **2013**, *3*, 3238.

(51) Liu, Y.; Penev, E. S.; Yakobson, B. I. Probing The Synthesis of Two-Dimensional Boron by First-Principles Computations. *Angew. Chem. Int. Ed.* **2013**, *52*, 3156–3159.

(52) Zhang, Z. H.; Yang, Y.; Gao, G. Y.; Yakobson, B. I. Two-Dimensional Boron Monolayers Mediated by Metal Substrates. *Angew. Chem. Int. Ed.* **2015**, *54*, 13022–13026.

(53) Zhao, J. H.; Yang, Z. Y.; Wei, N.; Kou, L. Z. Superhigh Moduli and Tension-Induced Phase Transition of Monolayer Gamma-Boron at Finite Temperatures. *Sci. Rep.* **2016**, *6*, 23233.

(54) Mir, S. H.; Chakraborty, S.; Jha, P. C.; Wärnå, J.; Soni, H.; Jha, P. K.; Ahuja, R. Two-Dimensional Boron: Lightest Catalyst for Hydrogen and Oxygen Evolution Reaction. *Appl. Phys. Lett.* **2016**, *109*, 053903.

(55) Zhang, Z.; Mannix, A. J.; Hu, Z.; Kiraly, B.; Guisinger, N. P.; Hersam, M. C.; Yakobson, B. I. Substrate-Induced Nanoscale Undulations of Borophene on Silver. *Nano Lett.* **2016**, *16*, 6622–6627.

(56) Jiao, Y. L.; Ma, F. X.; Bell, J.; Bilic, A.; Du, A. J. Two-Dimensional Boron Hydride Sheets: High Stability, Massless Dirac Fermions, and Excellent Mechanical Properties. *Angew. Chem. Int. Ed.* **2016**, *55*, 10292–10295.

(57) Matte, H. S.; Gomathi, A.; Manna, A. K.; Late, D. J.; Datta, R.; Pati, S. K.; Rao, C. N. MoS_2 and WS_2 Analogues of Graphene. *Angew. Chem. Int. Ed.* **2010**, *49*, 4059–4062.

(58) Yasaei, P.; Kumar, B.; Foroozan, T.; Wang, C.; Asadi, M.; Tuschel, D.; Indacochea, J. E.; Klie, R. F.; Salehi-Khojin, A. High-Quality Black Phosphorus Atomic Layers by Liquid-Phase Exfoliation. *Adv. Mater.* **2015**, *27*, 1887–1892.

(59) Smith, R. J.; King, P. J.; Lotya, M.; Wirtz, C.; Khan, U.; De, S.; O'Neill, A.; Duesberg, G. S.; Grunlan, J. C.; Moriarty, G.; Chen, J.; Wang, J.; Minett, A. I.; Nicolosi, V.; Coleman, J. N. Large-Scale Exfoliation of Inorganic Layered Compounds in Aqueous Surfactant Solutions. *Adv. Mater.* **2011**, *23*, 3944–3948.

(60) Lin, S.; Liu, S.; Yang, Z.; Li, Y.; Ng, T. W.; Xu, Z.; Bao, Q.; Hao, J.; Lee, C.-S.; Surya, C.; Yan, F.; Lau, S. P. Solution-Processable Ultrathin Black Phosphorus as an Effective Electron Transport Layer in Organic Photovoltaics. *Adv. Funct. Mater.* **2016**, *26*, 864–871.

(61) Nicolosi, V.; Chhowalla, M.; Kanatzidis, M. G.; Strano, M. S.; Coleman, J. N. Liquid Exfoliation of Layered Materials. *Science* **2013**, *340*, 1226419–1226437.

(62) Coleman, J. N.; Lotya, M.; O'Neill, A.; Bergin, S. D.; King, P. J.; Khan, U.; Young, K.; Gaucher, A.; De, S.; Smith, R. J.; Shvets, I. V.; Arora, S. K.; Stanton, G.; Kim, H. Y.; Lee, K.;

Kim, G. T.; Duesberg, G. S.; Hallam, T.; Boland, J. J.; Wang, J. J.; *et al*. Two-Dimensional Nanosheets Produced by Liquid Exfoliation of Layered Materials. *Science* **2011**, *331*, 568–571.

(63) Backes, C.; Higgins, T. M.; Kelly, A.; Boland, C.; Harvey, A.; Hanlon, D.; Coleman, J. N. Guidelines for Exfoliation, Characterization and Processing of Layered Materials Produced by Liquid Exfoliation. *Chem. Mater.* **2017,** *29*, 243–255.

(64) Ipus, J. J.; Blázquez, J. S.; Lozano-Perez, S.; Conde, A. Microstructural Evolution Characterization of Fe–Nb–B Ternary Systems Processed by Ball Milling. *Philos. Mag.* **2009**, *89*, 1415–1423.

(65) Zhan, C.; Zhang, P. F.; Dai, S.; Jiang, D. E. Boron Supercapacitors. *ACS Energy Lett.* **2016**, *1*, 1241–1246.

(66) Jiang, H.; Li, C. Z.; Sun, T.; Ma, J. A. Green and High Energy Density Asymmetric Supercapacitor Based on Ultrathin MnO_2 Nanostructures and Functional Mesoporous Carbon Nanotube Electrodes. *Nanoscale* **2012**, *4*, 807–812.

(67) Shao, Y. L.; Wang, H. Z.; Zhang, Q. H.; Li, Y. G. High-Performance Flexible Asymmetric Supercapacitors Based on 3D Porous Graphene/MnO_2 Nanorod and Graphene/Ag Hybrid Thin-Film Electrodes. *J. Mater. Chem. C* **2013**, *1*, 1245–1251.

(68) Lu, X. H.; Yu, M. H.; Wang, G. M.; Zhai, T.; Xie, S. L.; Ling, Y. C.; Tong, Y. X.; Li, Y. H-TiO_2@MnO_2//H-TiO_2@C Core-Shell Nanowires for High Performance and Flexible Asymmetric Supercapacitors. *Adv. Mater.* **2013**, *25*, 267–272.

(69) Liu, W. W.; Yan, X. B.; Lang, J. W.; Xue, Q. J. Electrochemical Behavior of Graphene Nanosheets in Alkylimidazolium Tetrafluoroborate Ionic Liquid Electrolytes: Influences of Organic Solvents and the Alkyl Chains. *J. Mater. Chem.* **2011**, *21*, 13205–13212.

(70) Chen, Y.; Zhang, X. O.; Zhang, D. C.; Yu, P.; Ma, Y. W. High Performance Supercapacitors Based on Reduced Graphene Oxide in Aqueous and Ionic Liquid Electrolytes. *Carbon* **2011**, *49*, 573–580.

(71) Lei, Z. B.; Liu, Z. H.; Wang, H. J.; Sun, X. X.; Lu, L.; Zhao, X. S. A High-Energy-Density Supercapacitor with Graphene-CMK-5 as the Electrode and Ionic Liquid as the Electrolyte. *J. Mater. Chem. A* **2013**, *1*, 2313–2321.

(72) Zhong, H.; Xu, F.; Li, Z. H.; Fu, R. W.; Wu, D. C. High-Energy Supercapacitors Based on Hierarchical Porous Carbon with an Ultrahigh Ion-Accessible Surface Area in Ionic Liquid Electrolytes. *Nanoscale* **2013**, *5*, 4678–4682.

(73) Jiang, H. R.; Lu, Z. H.; Wu, M. C.; Ciucci, F.; Zhao, T. S. Borophene: A Promising Anode Material Offering High Specific Capacity and High Rate Capability for Lithium-Ion Batteries. *Nano Energy* **2016**, *23*, 97–104.

(74) Jena, N. K.; Araujo, R. B.; Shukla, V.; Ahuja, R. Borophane as A Benchmate of Graphene: A Potential 2D Material for Anode of Li and Na-Ion Batteries. *ACS Appl. Mater. Inter.* **2017**, *9*, 16148–16158.

(75) Shi, L.; Zhao, T. S. Recent Advances in Inorganic 2D Materials and Their Applications in Lithium and Sodium Batteries. *J. Mater. Chem. A* **2017**, *5*, 3735–3758.

(76) Liu, W. W.; Yan, X. B.; Lang, J. W.; Peng, C.; Xue, Q. J. Flexible and Conductive Nanocomposite Electrode Based on Graphene Sheets and Cotton Cloth for Supercapacitor. *J. Mater. Chem.* **2012**, *22*, 17245–17253.

(77) Zhang, J. T.; Jiang, J. W.; Li, H. L.; Zhao, X. S. A High-Performance Asymmetric Supercapacitor Fabricated with Graphene-Based Electrodes. *Energ. Environ. Sci.* **2011**, *4*, 4009–4015.

(78) Yan, J.; Fan, Z. J.; Sun, W.; Ning, G. Q.; Wei, T.; Zhang, Q.; Zhang, R. F.; Zhi, L. J.; Wei, F. Advanced Asymmetric Supercapacitors Based on $Ni(OH)_2$/Graphene and Porous Graphene Electrodes with High Energy Density. *Adv. Funct. Mater.* **2012**, *22*, 2632–2641.

(79) Li, Z.; Liu, J.; Jiang, K. R.; Thundat, T. Carbonized Nanocellulose Sustainably Boosts the Performance of Activated Carbon in Ionic Liquid Supercapacitors. *Nano Energy* **2016**, *25*, 161–169.

(80) Gong, Y. N.; Li, D. L.; Luo, C. Z.; Fu, Q.; Pan, C. X. Highly Porous Graphitic Biomass Carbon as Advanced Electrode Materials for Supercapacitors. *Green Chem.* **2017**, *19*, 4132–4140.

(81) Guo, N. N.; Li, M.; Sun, X. K.; Wang, F.; Yang, R. Enzymatic Hydrolysis Lignin Derived Hierarchical Porous Carbon for Supercapacitors in Ionic Liquids with High Power and Energy Densities. *Green Chem.* **2017**, *19*, 2595–2602.

FIGURE CAPTIONS

Figure 1. (a) Schematic illustration of sonication-assisted liquid-phase exfoliation process. First, bulk B powder with an average lateral particle size of 2 μm was immersed into DMF/IPA (1 mg mL^{-1}) and was sonicated at 350 W for 4 h. Afterward, the supernatant was centrifuged at 5000 rpm for 30 min to remove unexfoliated B particles. Finally, stable, light-brown-colored dispersions in both DMF and IPA were obtained. SEM images of bulk B (b), B sheets obtained by tip-sonication in DMF (c), and IPA (d) for 4 h followed by centrifugation at 5000 rpm for 30 min, indicating the exfoliation of the bulk B. The insets of (c) and (d) show the corresponding photographs of a B sheet dispersion in DMF (a) and IPA, respectively.

Figure 2. Optical characterization of the few-layer B sheet dispersions. Photographs of B sheet dispersions in DMF (a) and IPA (d) after sonication for 4 h as well as after further centrifugation at different centrifugation speeds of 2000, 5000, and 12000 rpm for 30 min, respectively. Optical absorbance (A, at $\lambda = 400$ nm for DMF and $\lambda = 504$ nm for IPA) divided by cell length (l) as a function of concentration of DMF-exfoliated (b) and IPA-exfoliated (e) B sheet dispersions, which are consistent with the Lambert–Beer law, giving the absorption coefficient $\alpha = 704.38$ L g^{-1} m^{-1} for DMF and $\alpha = 977.55$ L g^{-1} m^{-1} for IPA, respectively. Their corresponding insets show the Tyndall effect of the B sheet dispersions after centrifugation at 5000 rpm for 30 min, indicating their colloidal nature. Tauc plots based on the optical absorption data from the DMF-exfoliated (c) and IPA-exfoliated (f) few-layer B sheet dispersions obtained at different centrifugation speeds of 5000 and 12000 rpm for 30 min.

Figure 3. AFM characterization of the B sheets obtained by tip-sonication in DMF (a-c) and IPA (d-f) for 4 h followed by centrifugation at 5000 rpm for 30 min, respectively. (a,d) Representative AFM topographic images and the corresponding height profiles. Statistical

data for 180 B sheets showing the average thickness (b) and area (c) of the DMF-exfoliated B sheets are 1.8 nm (corresponding to *ca*. 4 B layers) and 19827 nm^2, while the IPA-exfoliated B sheets possess a larger mean thickness (e) of 4.7 nm (corresponding to ca. 11 B layers) and smaller mean area (f) of 1791 nm^2, respectively.

Figure 4. Morphological and structural characterizations. Typical TEM images of the few-layer B sheets prepared by tip-sonication in DMF (a-c) and IPA (d-f) for 4 h followed by centrifugation at 5000 rpm for 30 min, respectively. Insets of (b), (e), and (f) show the corresponding FFT patterns of the selected areas. The uniform lattice fringes demonstrate that the crystalline state of the few-layer B sheets after the liquid-phase exfoliation process is pristine. HAADF STEM and corresponding EELS elemental mapping images of the few-layer B sheets prepared by tip-sonication in DMF (g-k) and IPA (l-p) for 4 h followed by centrifugation at 5000 rpm for 30 min, showing the uniform distribution of B element throughout the whole sheet with an observable shell consisting of C, N, and O elements. (q) EELS spectra of the exfoliated few-layer B sheets. (r) XRD patterns of the B before and after exfoliation using DMF and IPA as exfoliating solvents, indicating both the DMF- and IPA-exfoliated few-layer B sheets retain the crystallinity of the original bulk B.

Figure 5. XPS characterization of bulk B, few-layer B sheets after sonication in DMF, and DMF- and IPA-exfoliated few-layer B sheets after centrifugation at 5000 rpm for 30 min. (a) Survey spectra (upper part) and the corresponding atomic ratios (lower part). It is noted that there is no obvious change in the B content for all four B samples, indicating the surface composition can be well retained after the sonication-assisted liquid-phase exfoliation process. High-resolution spectra of (b) B 1s and (c) C 1s, respectively. The high-resolution B 1s spectra of the DMF- and IPA-exfoliated few-layer B sheets show that most B atoms remain intact after the sonication-assisted liquid-phase exfoliation process. This is also supported by

the measured ratio of the C-B peak (282.8 eV) for DMF- and IPA-exfoliated few-layer B sheets, which is only ~0.033 and ~0.058, respectively.

Figure 6. Optical absorption spectra of the fresh DMF-exfoliated B sheet dispersions and the corresponding dispersions after 50 days of exposure to ambient conditions obtained by centrifugation at 5000 rpm (a) and 12000 rpm (b) for 30 min, respectively. The inset of (a) shows that DMF-exfoliated B sheet dispersion after 50 days of exposure to ambient conditions still exhibits an obvious Tyndall effect. The inset of (b) shows the corresponding optical band gap. There is almost no change in the spectra of the DMF-exfoliated B sheet dispersions, indicating excellent stability of the as-prepared colloid.

Figure 7. Electrochemical performance of DMF-exfoliated few-layer B sheets based supercapacitor in ionic liquid electrolyte. (a) CV curves collected under various voltage windows at a scan rate of 10 mV/s. (b) CV curves tested at different scan rates. (c) Galvanostatic charge/discharge curves at various current densities. (d) Variation of specific capacitance and cell capacitance at different current densities. (e) Cycling performance of the as-prepared supercapacitor collected at a scan rate of 50 mV/s for 6000 cycles. (f) Nyquist plots before and after 6000 cycles. (g) Ragone plot compared with those of reported supercapacitors based on other carbon materials in ionic liquid. Photographs of the obtained coin cell powering (h) one red LED light and (i) one mini-fan.

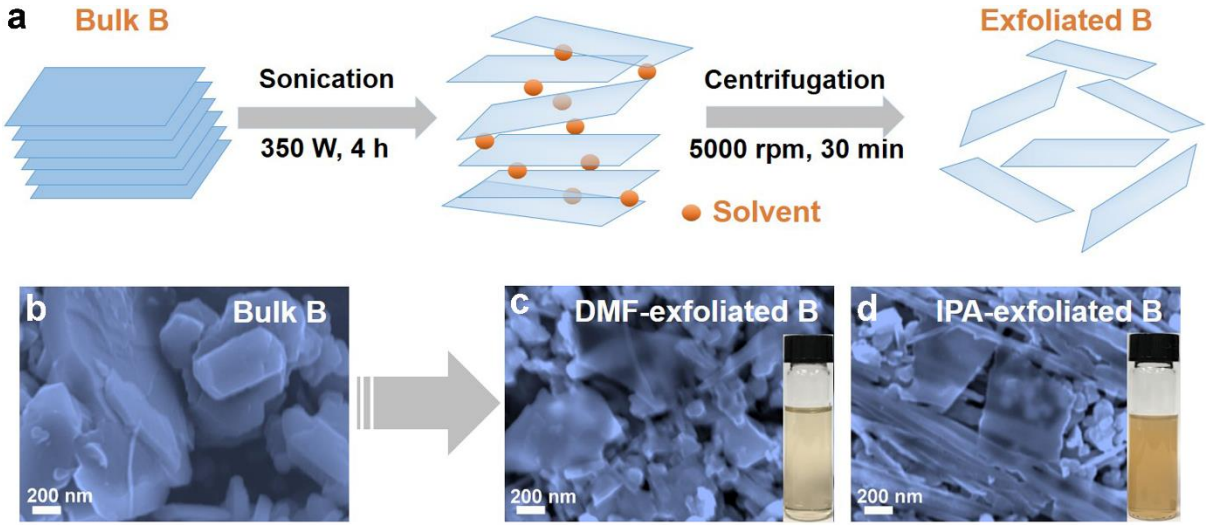

Figure 1. (a) Schematic illustration of sonication-assisted liquid-phase exfoliation process. First, bulk B powder with an average lateral particle size of 2 µm was immersed into DMF/IPA (1 mg mL^{-1}) and was sonicated at 350 W for 4 h. Afterward, the supernatant was centrifuged at 5000 rpm for 30 min to remove unexfoliated B particles. Finally, stable, light-brown-colored dispersions in both DMF and IPA were obtained. SEM images of bulk B (b), B sheets obtained by tip-sonication in DMF (c), and IPA (d) for 4 h followed by centrifugation at 5000 rpm for 30 min, indicating the exfoliation of the bulk B. The insets of (c) and (d) show the corresponding photographs of a B sheet dispersion in DMF (a) and IPA, respectively.

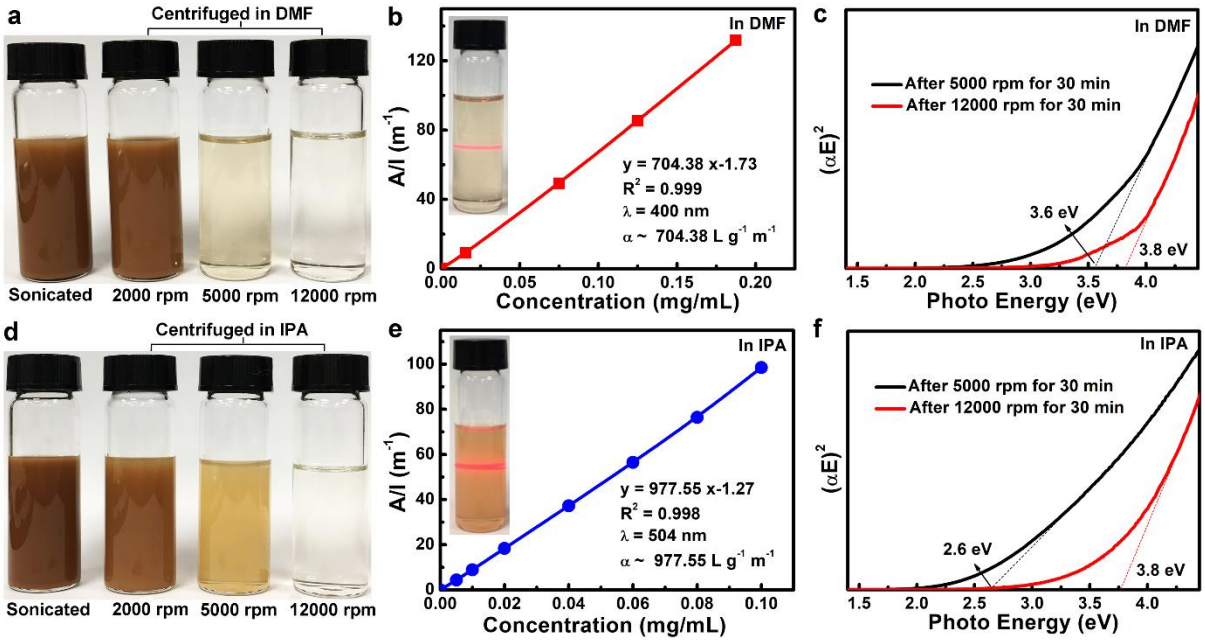

Figure 2. Optical characterization of the few-layer B sheet dispersions. Photographs of B sheet dispersions in DMF (a) and IPA (d) after sonication for 4 h as well as after further centrifugation at different centrifugation speeds of 2000, 5000, and 12000 rpm for 30 min, respectively. Optical absorbance (*A*, at λ = 400 nm for DMF and λ = 504 nm for IPA) divided by cell length (*l*) as a function of concentration of DMF-exfoliated (b) and IPA-exfoliated (e) B sheet dispersions, which are consistent with the Lambert–Beer law, giving the absorption coefficient α = 704.38 L g^{-1} m^{-1} for DMF and α = 977.55 L g^{-1} m^{-1} for IPA, respectively. Their corresponding insets show the Tyndall effect of the B sheet dispersions after centrifugation at 5000 rpm for 30 min, indicating their colloidal nature. Tauc plots based on the optical absorption data from the DMF-exfoliated (c) and IPA-exfoliated (f) few-layer B sheet dispersions obtained at different centrifugation speeds of 5000 and 12000 rpm for 30 min.

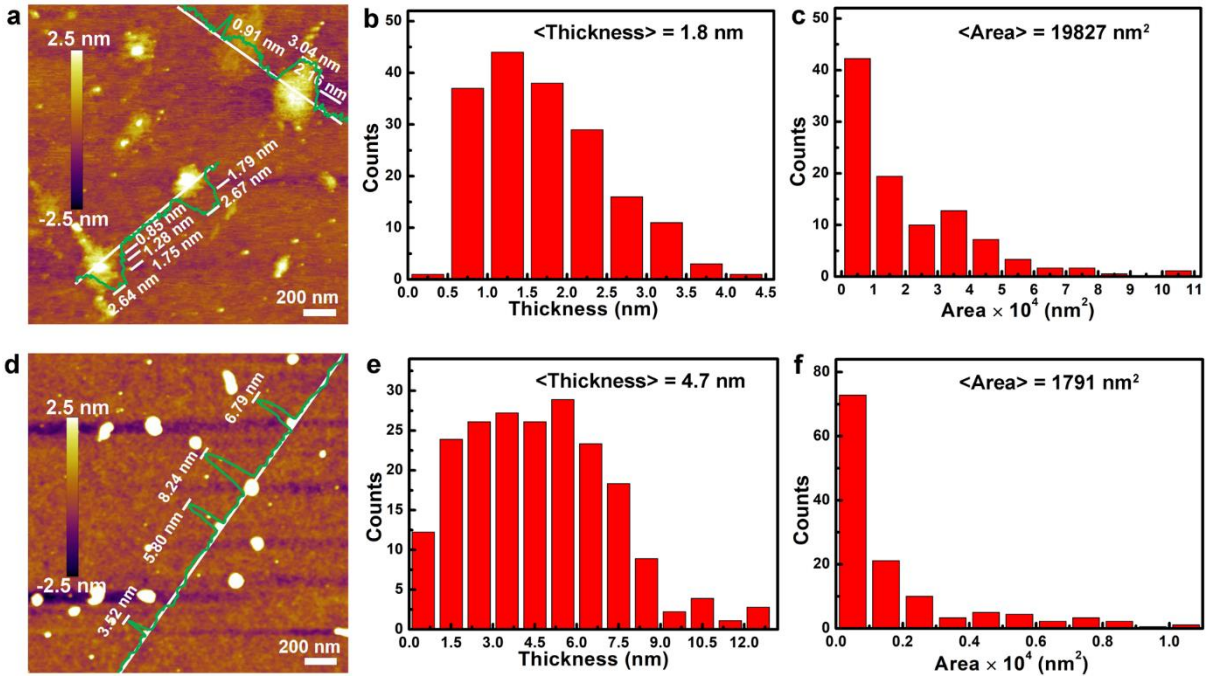

Figure 3. AFM characterization of the B sheets obtained by tip-sonication in DMF (a-c) and IPA (d-f) for 4 h followed by centrifugation at 5000 rpm for 30 min, respectively. (a,d) Representative AFM topographic images and the corresponding height profiles. Statistical data for 180 B sheets showing the average thickness (b) and area (c) of the DMF-exfoliated B sheets are 1.8 nm (corresponding to *ca*. 4 B layers) and 19827 nm^2, while the IPA-exfoliated B sheets possess a larger mean thickness (e) of 4.7 nm (corresponding to ca. 11 B layers) and smaller mean area (f) of 1791 nm^2, respectively.

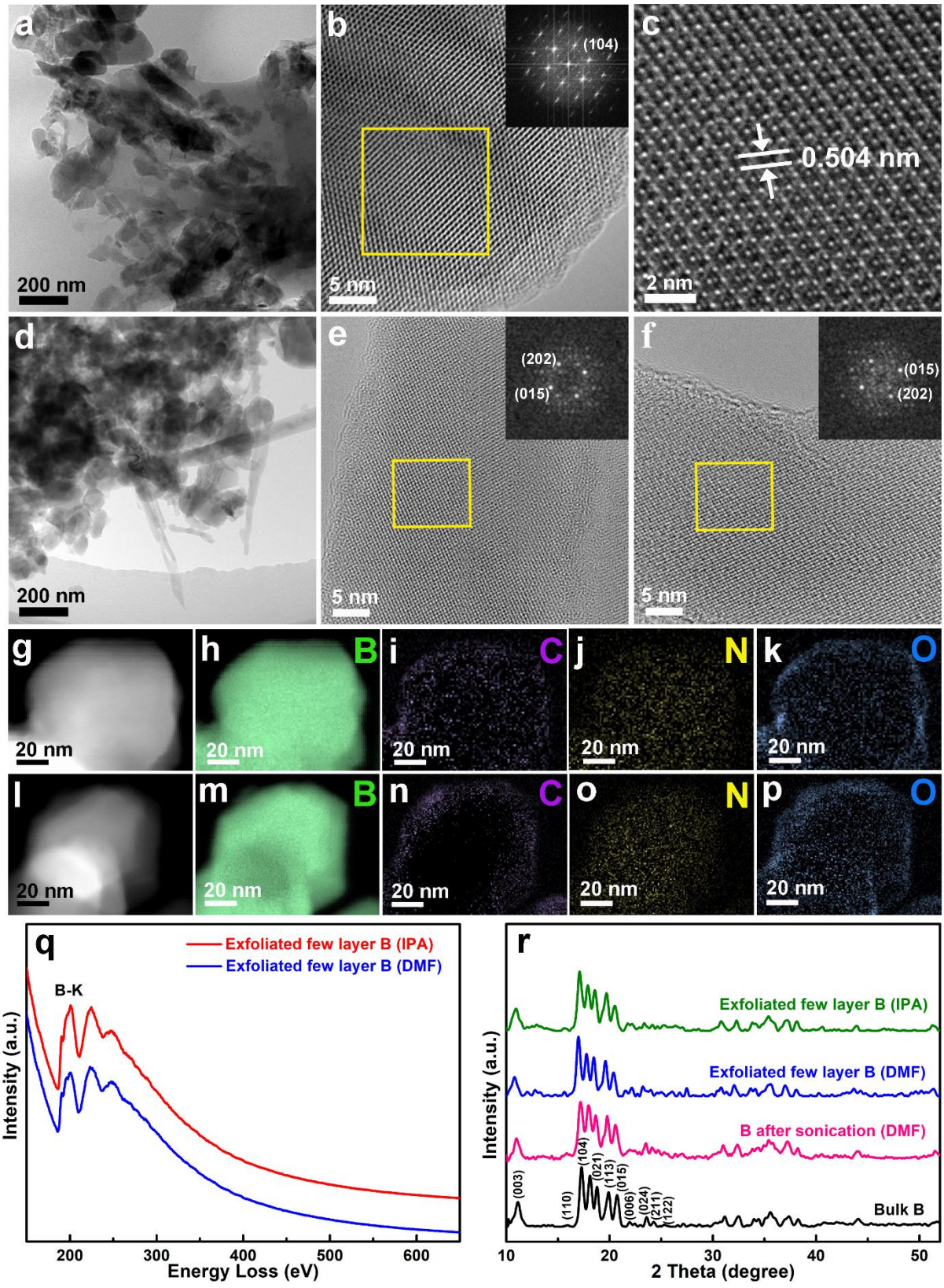
a
200 nm
b
(104)
5 nm
c
0.504 nm
2 nm
d
200 nm
e
(202)
(015)
5 nm
f
(015)
(202)
5 nm
g
20 nm
h
B
20 nm
i
C
20 nm
j
N
20 nm
k
O
20 nm
l
20 nm
m
B
20 nm
n
C
20 nm
o
N
20 nm
p
O
20 nm
q
Exfoliated few layer B (IPA)
Exfoliated few layer B (DMF)
B-K
Intensity (a.u.)
200
300
400
500
600
Energy Loss (eV)
r
Exfoliated few layer B (IPA)
Exfoliated few layer B (DMF)
B after sonication (DMF)
Bulk B
(003)
(110)
(104)
(021)
(113)
(015)
(006)
(024)
(211)
(122)
Intensity (a.u.)
10
20
30
40
50
2 Theta (degree)

Figure 4. Morphological and structural characterizations. Typical TEM images of the few-layer B sheets prepared by tip-sonication in DMF (a-c) and IPA (d-f) for 4 h followed by centrifugation at 5000 rpm for 30 min, respectively. Insets of (b), (e), and (f) show the corresponding FFT patterns of the selected areas. The uniform lattice fringes demonstrate that the crystalline state of the few-layer B sheets after the liquid-phase exfoliation process is pristine. HAADF STEM and corresponding EELS elemental mapping images of the few-layer B sheets prepared by tip-sonication in DMF (g-k) and IPA (l-p) for 4 h followed by centrifugation at 5000 rpm for 30 min, showing the uniform distribution of B element throughout the whole sheet with an observable shell consisting of C, N, and O elements. (q) EELS spectra of the exfoliated few-layer B sheets. (r) XRD patterns of the B before and after exfoliation using DMF and IPA as exfoliating solvents, indicating both the DMF- and IPA-exfoliated few-layer B sheets retain the crystallinity of the original bulk B.

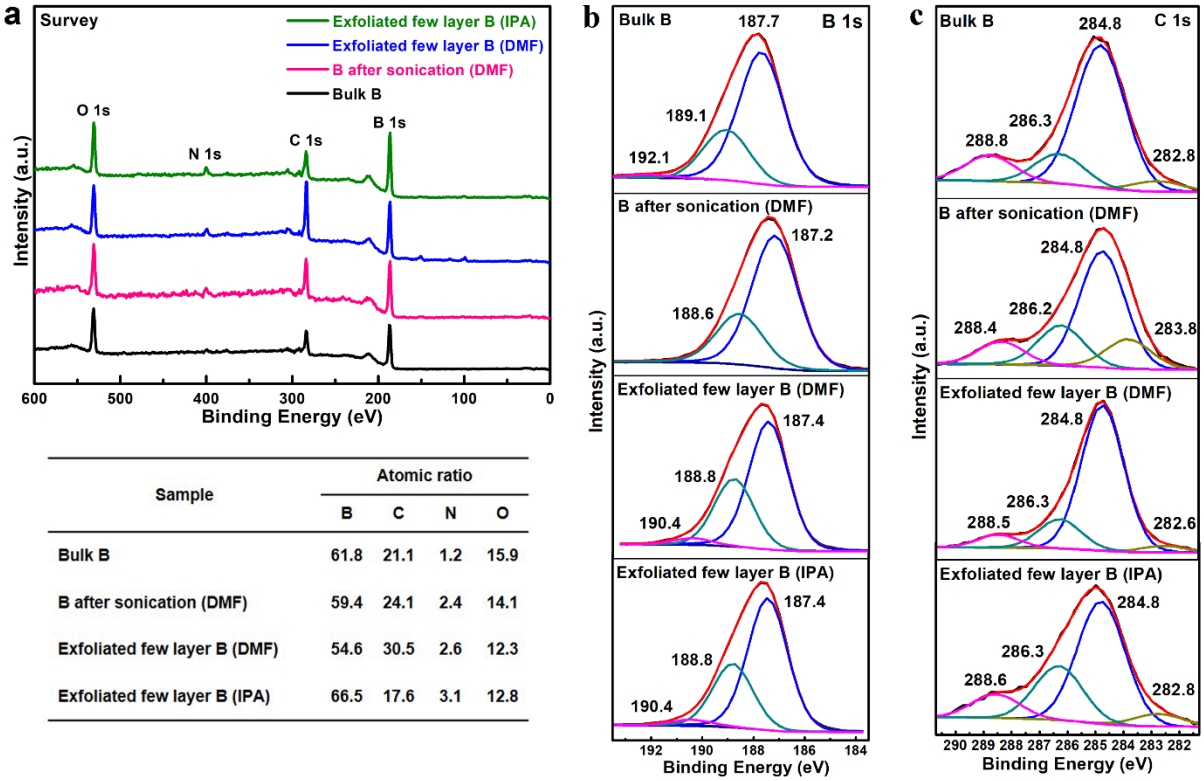

Sample	Atomic ratio			
	B	C	N	O
Bulk B	61.8	21.1	1.2	15.9
B after sonication (DMF)	59.4	24.1	2.4	14.1
Exfoliated few layer B (DMF)	54.6	30.5	2.6	12.3
Exfoliated few layer B (IPA)	66.5	17.6	3.1	12.8

Figure 5. XPS characterization of bulk B, few-layer B sheets after sonication in DMF, and DMF- and IPA-exfoliated few-layer B sheets after centrifugation at 5000 rpm for 30 min. (a) Survey spectra (upper part) and the corresponding atomic ratios (lower part). It is noted that there is no obvious change in the B content for all four B samples, indicating the surface composition can be well retained after the sonication-assisted liquid-phase exfoliation process. High-resolution spectra of (b) B 1s and (c) C 1s, respectively. The high-resolution B 1s spectra of the DMF- and IPA-exfoliated few-layer B sheets show that most B atoms remain intact after the sonication-assisted liquid-phase exfoliation process. This is also supported by the measured ratio of the C-B peak (282.8 eV) for DMF- and IPA-exfoliated few-layer B sheets, which is only ~0.033 and ~0.058, respectively.

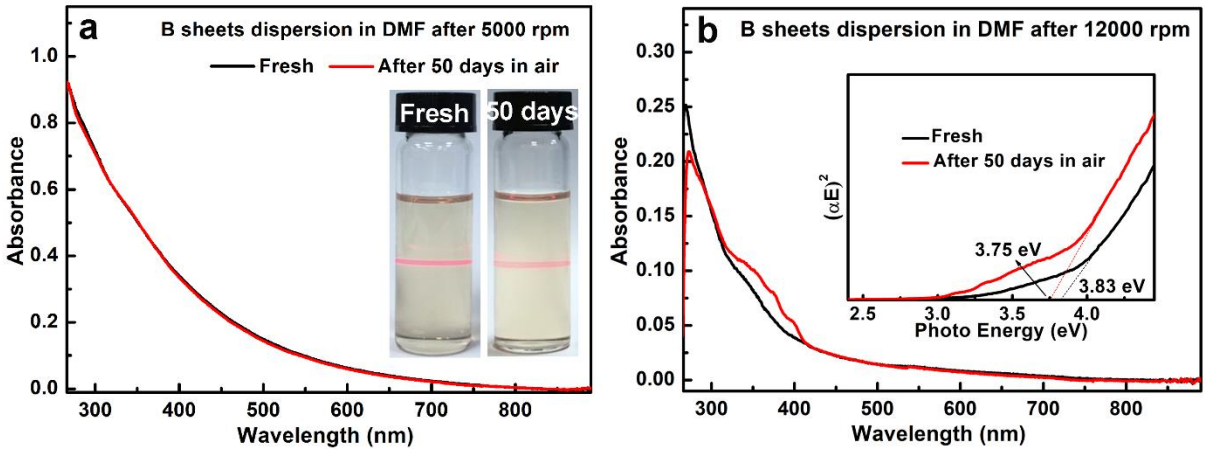

Figure 6. Optical absorption spectra of the fresh DMF-exfoliated B sheet dispersions and the corresponding dispersions after 50 days of exposure to ambient conditions obtained by centrifugation at 5000 rpm (a) and 12000 rpm (b) for 30 min, respectively. The inset of (a) shows that DMF-exfoliated B sheet dispersion after 50 days of exposure to ambient conditions still exhibits an obvious Tyndall effect. The inset of (b) shows the corresponding optical band gap. There is almost no change in the spectra of the DMF-exfoliated B sheet dispersions, indicating excellent stability of the as-prepared colloid.

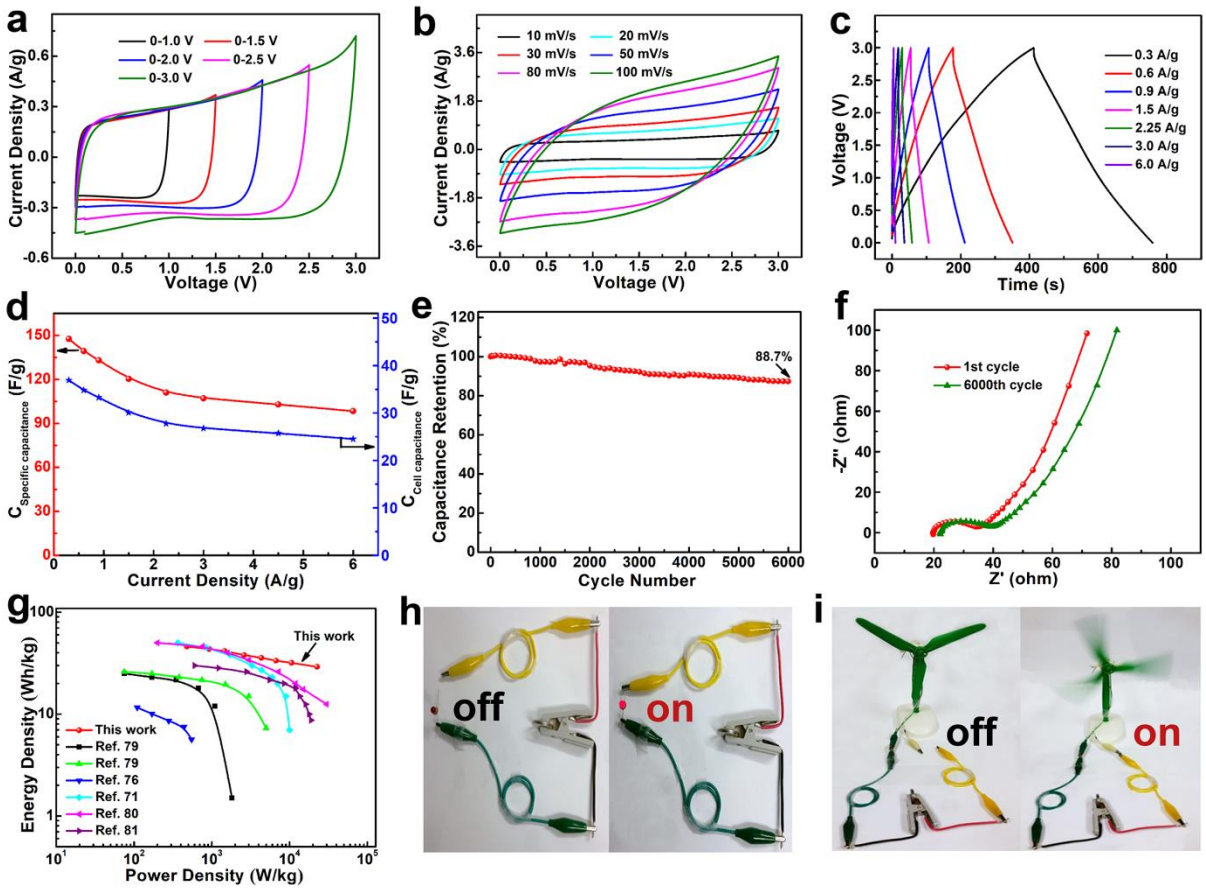

Figure 7. Electrochemical performance of DMF-exfoliated few-layer B sheets based supercapacitor in ionic liquid electrolyte. (a) CV curves collected under various voltage windows at a scan rate of 10 mV/s. (b) CV curves tested at different scan rates. (c) Galvanostatic charge/discharge curves at various current densities. (d) Variation of specific capacitance and cell capacitance at different current densities. (e) Cycling performance of the as-prepared supercapacitor collected at a scan rate of 50 mV/s for 6000 cycles. (f) Nyquist plots before and after 6000 cycles. (g) Ragone plot compared with those of reported supercapacitors based on other carbon materials in ionic liquid. Photographs of the obtained coin cell powering (h) one red LED light and (i) one mini-fan.

Graphical Table of Contents

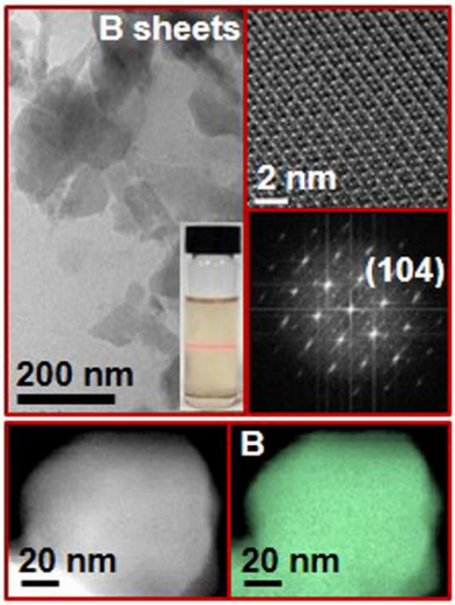

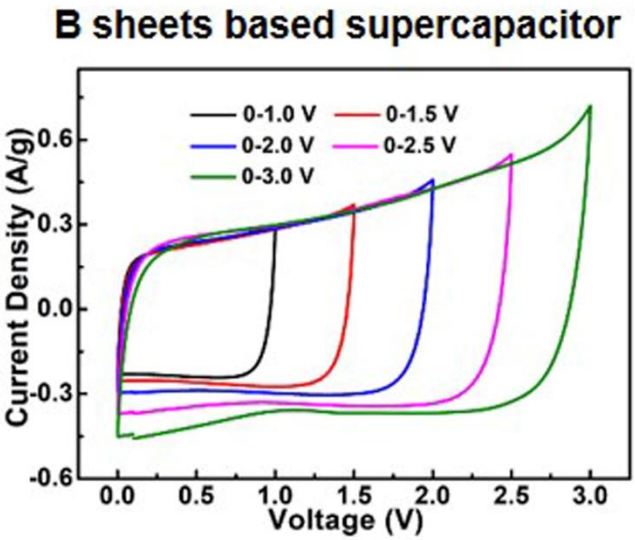

SUPPORTING INFORMATION

Scalable Production of Few-Layer Boron Sheets by Liquid-Phase Exfoliation and Their Superior Supercapacitive Performance

Hongling Li,[1,⊥] Lin Jing,[2,⊥] Wenwen Liu,[3] Jinjun Lin,[1] Roland Yingjie Tay,[4] Siu Hon Tsang,[4] and Edwin Hang Tong Teo [1,2,*]

[1]School of Electrical and Electronic Engineering, Nanyang Technological University, 50 Nanyang Avenue, Singapore 639798, Singapore

[2]School of Materials Science and Engineering, Nanyang Technological University, 50 Nanyang Avenue, Singapore 639798, Singapore

[3]Department of Chemical Engineering, Waterloo Institute for Nanotechnology, University of Waterloo, Waterloo, Ontario, Canada N2L 3G1

[4]Temasek Laboratories@NTU, 50 Nanyang Avenue, Singapore 639798, Singapore

*Corresponding Author. *E-mail:* HTTEO@ntu.edu.sg

⊥These two authors contributed equally to this work.

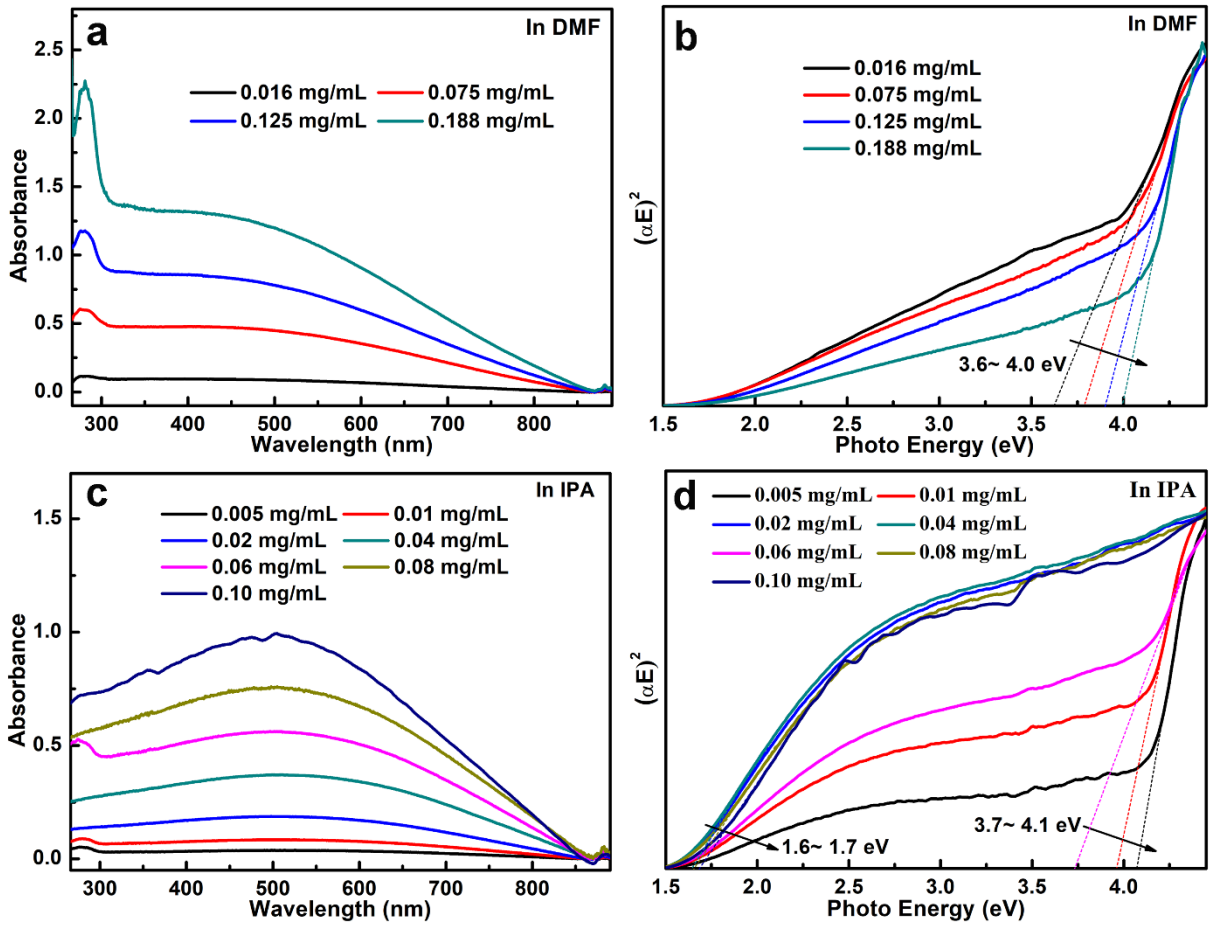

Figure S1. Optical absorption spectra and the corresponding optical band gap of redispersed B sheet dispersions in (a, b) DMF and (c, d) IPA with different concentrations. The results indicate the DMF-exfoliated B sheets show much better stability and redispersion properties while the IPA-exfoliated B sheets are more likely to reaggregate.

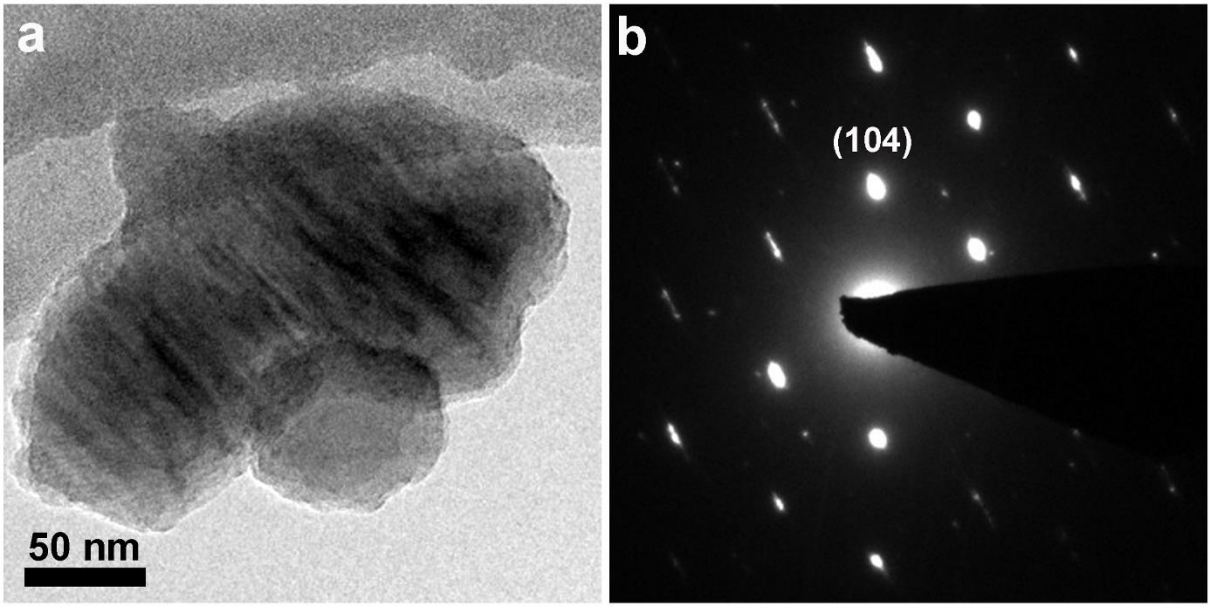

Figure S2. Typical TEM image (a) of the few-layer B sheets exfoliated in DMF at lower magnification and the corresponding selected-area electron diffraction (SAED) pattern.

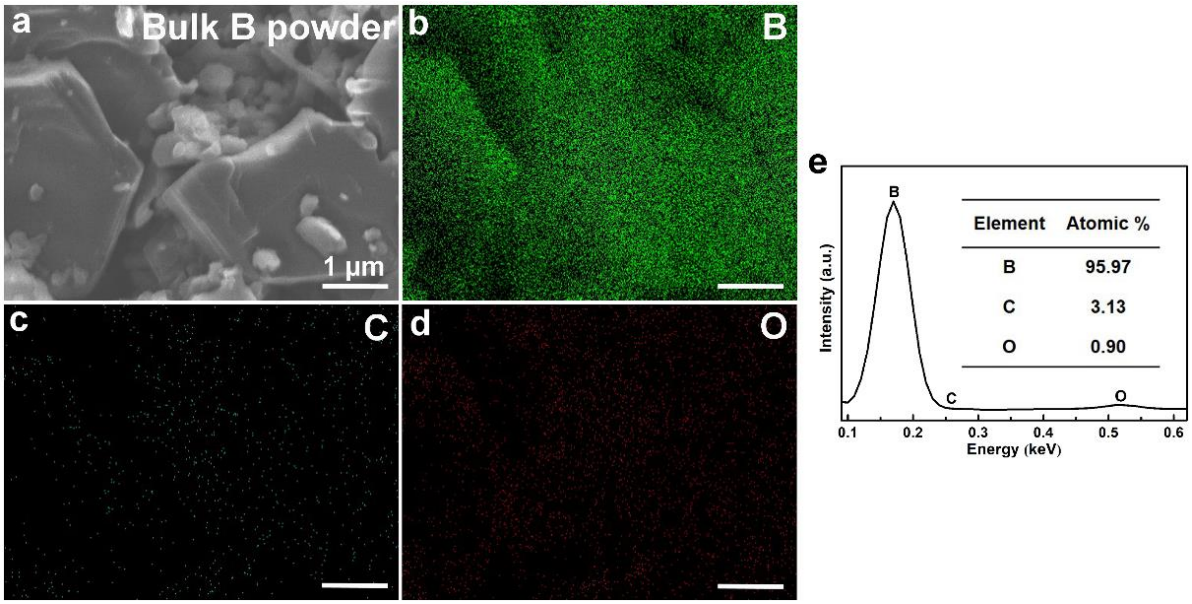

Figure S3. Typical (a) SEM, corresponding elemental mapping images of (b) B, (c) C, (d) O, and (e) EDX spectrum of the bulk B, showing a uniform distribution of B element at a very high density and random distribution of C and O elements at a very low density throughout the whole area. The inset of (e) shows the atomic ratio of the elements B, C and O, respectively, indicating the bulk B consists mainly of B element with the presence of a small amount of C and O impurities.

SEM-EDX elemental analysis was performed to visually demonstrate the elemental spatial distribution of the bulk B (Figure S3). Three elements including B, C and O were detected in the bulk B. It is noted that the B element is uniformly distributed throughout the whole area at a very high density (Figure S3b), while the C and O elements are randomly distributed within the area at a very low density (Figures S3c,d), indicating the bulk B consists mainly of B element with the presence of a small amount of C and O impurities. This is supported by the corresponding EDX spectrum of the bulk B and the extracted atomic ratio of the element B (95.97%, Figure S3e).

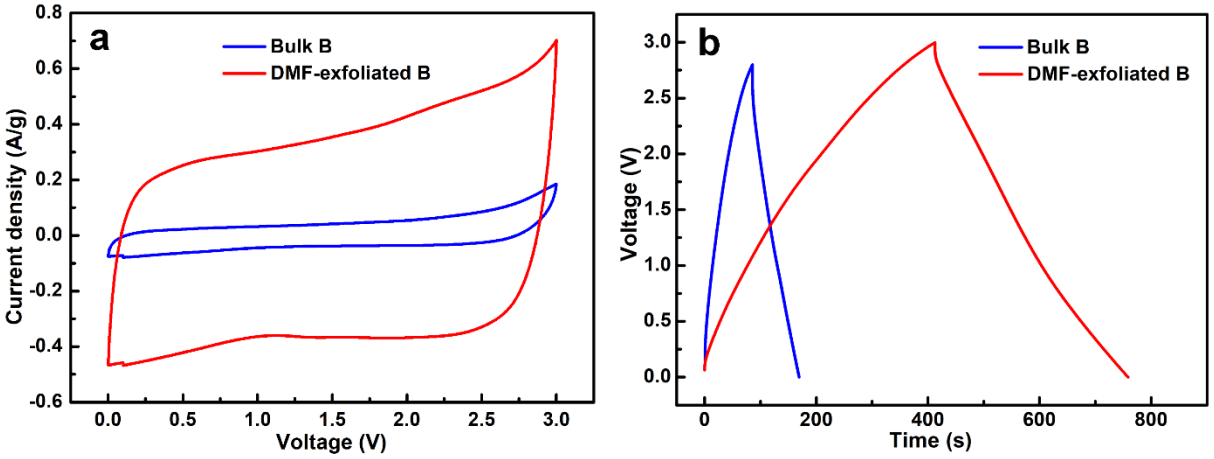

Figure S4. Comparison of electrochemical performance of bulk B and DMF-exfoliated few-layer B sheets based supercapacitor in ionic liquid electrolyte. (a) CV curves collected at a scan rate of 10 mV/s. (b) Galvanostatic charge/discharge curves at a current density of 0.3 A/g.